Journal of Heat and Mass Transfer Research 5 (2018) 11-26

Journal of Heat and Mass Transfer Research

Journal homepage: http://jhmtr.journals.semnan.ac.ir

Semnan University

A numerical investigation of heat transfer and pressure drop in a novel cylindrical heat sink with helical minichannels

Alireza Falahat, Reza Bahoosh*, Aminreza Noghrehabadi

Department of Mechanical Engineering, Shahid Chamran University of Ahvaz, Ahvaz, Iran

PAPER INFO

History:

Submitted2017-05-05
Revised 2017-07-07
Accepted 2017-07-12

Keywords :

Cylindrical helical minichannel heat sink;
Thermal performance factor;
Thermal resistance;
Entropy generation;
Channel aspect ratio.

A B S T R A C T

This study numerically investigated heat transfer and fluid flow characteristics in a novel cylindrical heat sink with helical minichannels for the laminar flow of fluid with temperature-dependent properties. A finite volume method was employed to obtain the solution of governing equations. The effects of helical angle, channel aspect ratio, and Reynolds number, which were regarded as main parameters, were determined. The overall performance of the heat sink was also analyzed on the basis of the thermal performance factor and the augmentation entropy generation number. Results showed that a decrease in the channel helix angle and an increase in the channel aspect ratio and Reynolds number enhance the average heat transfer coefficient and pressure drop in the heat sink. The thermal performance factor and entropy generation minimization method revealed that an aspect ratio of 1.2 enables the best heat sink performance at all helix angles. When the helix angle decreases, performance increases, especially at low aspect ratios.

DOI: 10.22075/jhmtr.2017.1503.1100

1. Introduction

Effective cooling and thermal management are essential and inevitable requirements in high-energy applications, such as those associated with batteries, motors, microelectronics, and micro/mini reactors. In these devices, single-phase micro/minichannel liquid cooling is suitable for high heat flux dissipation because they have a high area-to-volume ratio, a large heat transfer coefficient, and a minimal requirement for coolant fluid. Conventional micro/minichannel heat sinks are characterized by poor flow mixing, thus rendering such equipment inadequate for effective heat transfer. An innovative solution to deficient heat transfer is the generation of secondary flow [1]. During the past two decades, many researchers have investigated several techniques for enhancing heat transfer in micro/minichannel heat sink, both theoretically and experimentally. Tukerman and Pease [2], for instance, studied microchannel cooling technology for heat dissipation in electronic cooling. The authors showed that a heat flux of 790 W/cm^2 can be eliminated through the cooling of water flow under a maximum temperature difference of 71°C between silicon substrate and inlet flow. Qu and Mudawer [3] investigated the heat transfer and pressure drop across a rectangular microchannel heat sink. The results revealed that the outlet temperature of cooling fluid decreases with increasing Reynolds number and increases along the flow direction for each Reynolds number. The authors also found that at a fixed Reynolds number, pressure drop increases with increasing Reynolds number and effective heat flux. Xie et al. [4] numerically studied the effects of geometrical parameters and fluid flow velocity on heat transfer and pressure drop in a minichannel heat

Corresponding Author: *R. Bahoosh , Department of Mechanical Engineering, Shahid Chamran University of Ahvaz, Ahvaz, Iran*
Email : bahoosh@scu.ac.ir

sink. The results indicated that pressure drop strongly depends on minichannel geometry. The authors further reported that a narrow channel enables more efficient heat transfer than does a wide channel. Laminar water flow in wavy microchannels with rectangular cross-sections was numerically investigated by Sui et al. [5], who found that secondary flow is generated by water flow in wavy microchannels. The authors concluded that in a fixed cross-section of the microchannels, heat transfer exhibits an improvement over the levels observed in straight microchannels. Mohammed et al. [6] numerically analyzed the heat transfer and pressure drop in a microchannel heat sink with differently shaped channels. They found that in a fixed cross-section of a microchannel, zigzag-shaped microchannels present the highest convective heat transfer coefficient and a maximum pressure drop. In another study [7], the authors numerically inquired into heat transfer and fluid flow in a wavy microchannel heat sink. They discovered that a decrease in the wave amplitude of the channel increases temperature and that the pressure drop in wavy microchannels is greater than that in straight microchannels. Lei et al. [8] also conducted a numerical investigation, with particular focus on heat transfer and fluid flow in a planar heat sink with sectional oblique fins. The results indicated that in designed oblique fins, the generation of secondary flow and the reduction of boundary layer thickness enhance heat transfer. Another numerical research was that conducted by Chai et al. [9], who probed into the heat transfer characteristics of fan-shaped ribs on the side wall of microchannel heat sinks under laminar flow. They found that the ribs impede increases in wall temperature and that the local heat transfer coefficient increases with decreasing fan-shaped spacing and increasing height. Xie et al.'s [10] study was devoted to heat transfer and fluid flow characteristics in microchannel heat sinks with rectangular flow obstructions. The researchers determined that heat transfer in the aforementioned heat sinks is greater than that in microchannels without flow obstructions. The authors added that the length of flow obstructions significantly affects the thermal performance of microchannel heat sinks. In numerically analyzing the heat transfer and fluid flow of Al_2O_3-ethylen glycol-water nanofluid in wavy microchannels, Zhu et al. [11] found that such channels feature efficient heat transfer performance but that the pressure drop is higher than that occurring in plain microchannels. They also discovered that at low volume concentrations of nanofluid, thermal performance is superior to that achieved at high volume concentrations. Bovand et al. [12] numerically explored the effects of several parameters on heat transfer and flow structure in a porous solar heater. The authors reported that the Nusselt number increases with the incorporation of porous substrate into the solar heater.

Numerical analysis can also be directed toward entropy generation as a powerful approach to investigating system performance. In this regard, Bashi et al. [13] employed a numerical approach to explore entropy generation in a porous triangular duct. The researchers found that total entropy generation increases with the incorporation of porous materials into the duct and that frictional entropy generation dominates in the porous channel. Rashidi et al. [14] numerically examined the thermofluidic performance and entropy generation of new eccentric helical screw tape inserts in circular tubes under a turbulent regime. They reported that the performance factor improves with increasing eccentricity values at all ranges of the Reynolds number. They likewise declared that total thermal and frictional entropy generation increases with rising eccentricity values and Reynolds numbers. Rashidi et al. [15] performed a numerical study of corrugated channels at different Reynolds numbers, wave amplitudes, and wavelengths under a turbulent regime. The specific object of the study was thermohydraulic and entropy generation in the channels. They found that overall performance improves because of the corrugated channel and that total entropy generation is at its minimum at all wave amplitude and wavelength ranges and at a Reynolds number of 20000.

A number of researchers have experimentally studied heat transfer and fluid flow in planar micro/minichannel heat sinks under laminar fluid flow. Examples are Ho et al. [16], Lee et al. [17], Rimbault et al. [18], Zirakzadeh et al. [19], Lee et al. [20], Peyghambarzadeh et al. [21], and Khoshvaght-Aliabadi and Nozan [22]. Most focused on planar micro/minichannel heat sinks, and fewer efforts have been devoted to the cooling of cylindrical heat sources, such as batteries, motors, and micro/mini reactors. Fan et al. [23, 24] experimentally and numerically delved into the heat transfer and fluid flow of water in a novel cylindrical minichannel heat sink. The minichannel heat sink, which also has cylindrical oblique fins, increases the average Nusselt number by 75.6% and decreases thermal resistance by 59.1%. Azizi et al. [25, 26] experimentally investigated the heat transfer and fluid flow of Cu-water nanofluid in a cylindrical microchannel heat sink. The maximum enhancement in the average Nusselt number is 23% at a 0.3% mass fraction of nanoparticles. The authors also reported that the entrance Nusselt number improves by 43% but that the friction factor increases by 45.5%.

The main aim of the present work was to numerically investigate heat transfer and fluid flow characteristics in a novel cylindrical heat sink with helical minichannels for laminar flow—issues that have not been explored in previous studies. The effects of helix angle, channel aspect ratio, and Reynolds number were investigated, and the heat

transfer performance of the heat sink was examined on the basis of the performance factor and the augmentation entropy generation number.

2. Methodology

2.1 Description of cylindrical heat sink with helical minichannels

Fig. 1 illustrates the physical model of the cylindrical heat sink and the computational domain pursued in this work. The cooling fluid and the material constituting the heat sink are water and copper, respectively. Each heat sink contains 36 minichannels with rectangular cross-sections. Four helix angles of the rectangular minichannels, namely, 45°, 60°, 75°, and 90° (straight minichannel), were considered. For each helix angle, six aspect ratios (*AR*) (i.e., 1, 1.2, 3.6, 7.2, 10.8, and 16.2) were chosen for the same cross-sectional area. All the parameters are presented in Table 1.

Table 1. Geometric parameters of minichannels at different aspect ratios (mm) A_C=1.2 mm^2, D = 25 mm, d = 10 mm.

Case Number	$AR=H/W$	H	W	D_h
1	1	1.095	1.095	1.095
2	1.2	1.2	1	1.091
3	3.6	2.078	0.577	0.904
4	7.2	2.939	0.408	0.717
5	10.8	3.6	0.333	0.610
6	16.2	4.409	0.272	0.513

2.2 Governing equations and boundary conditions

To analyze three-dimensional conjugate heat transfer in the cylindrical heat sink, the following assumptions were adopted: Flow is of a laminar, incompressible, and steady-state nature; natural convection, radiation, and viscous dissipation are negligible [27]; the thermophysical properties of fluids vary in a piecewise linear manner with fluid temperature [28]; and the thermophysical properties of solid are constant. In accordance with these assumptions, the governing equations for fluids and solids are as follows:

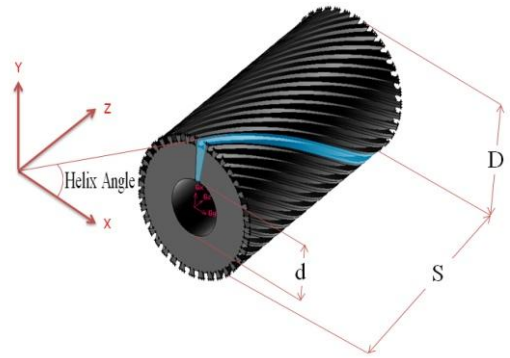

b)

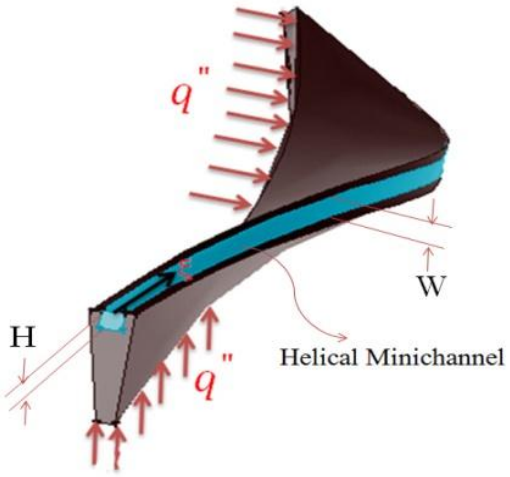

c)

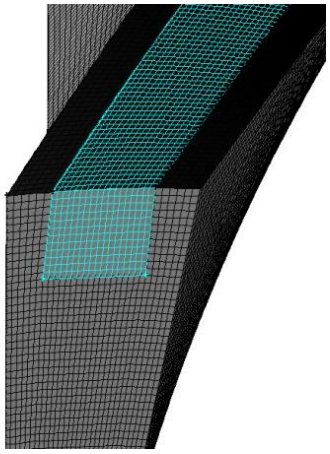

Fig. 1. Cylindrical heat sink with helical minichannels; (a) full domain, (b) computational domain, and (c) schematic view of the three-dimensional mesh.

a)

Continuity equation:

$$\nabla \cdot (V) = 0 \tag{1}$$

Momentum equation:

$$\rho(V \nabla \cdot V) = -\nabla P + \nabla \cdot (\mu \nabla V) \tag{2}$$

Energy equation for liquids:

$$V \cdot \nabla T = \frac{k}{\rho C_p} \nabla^2 T \tag{3}$$

Energy equation for solids:

$$\nabla^2 T = 0 \tag{4}$$

The hydraulic diameter can be expressed using the following equation [29]:

$$D_h = \frac{2HW}{H + W} = \frac{2H}{1 + AR} \tag{5}$$

where AR is the aspect ratio, and Re is the Reynolds number, expressed thus:

$$\mathrm{Re} = \frac{\rho v_{av} D_h}{\mu} = \frac{2\dot{m}}{\mu(W + H)} \tag{6}$$

in which v_{av} denotes the average velocity of fluids over the cross-sectional area of the minichannels, and $\dot{m}$ represents the inlet mass flow rate. The Darcy friction factor and pumping power are defined by

$$f = \frac{2\Delta P D_h}{\rho L v_{av}^2} \tag{7}$$

$$PP = \frac{\dot{m}}{\rho} \Delta P = n v_{av} A_C \Delta P \tag{8}$$

where ΔP, L, and n are the pressure drop in the minichannels, the length of the minichannels, and the number of minichannels, respectively.

The average Nusselt number and heat transfer coefficient are defined as

Table 2. Boundary conditions assigned for simulations.

Boundaries	**Conditions**
Minichannel inlet	Uniform mass flow rate with uniform temperature ($T_{in} = 297^o K$)
Minichannel outlet	Pressure outlet [31] ($P_{out,gage} = 0\ Pa$)
Bottom wall of substrate heat sink	$q^{"} = 2.5 \times 10^6\ W/m^2$
Side walls of substrate heat sink	*Periodic*
Both end walls of substrate heat sink and top wall of minichannels and fins	*Adiabatic*
Inner walls/fluid–solid interface	$-k_s \frac{\partial T_s}{\partial n} = -k_f \frac{\partial T_f}{\partial n}$ *and* $T_f = T_s$

$$Nu_{av} = \frac{h_{av} D_h}{k} \tag{9}$$

$$h_{av} = \frac{Q}{A_S (T_{W,av} - T_f)} \tag{10}$$

where Q is the heat transfer absorbed by water, A_s is the heat transfer area of the minichannels, $T_{w,av}$ is the average temperature of the minichannel wall, and $T_f = (T_{in} + T_{out})/2$ is the average temperature of a fluid.

Overall thermal resistance is an important parameter for the thermal performance evaluation of micro/minichannel heat sinks. Such parameter is obtained using [4, 30–32]

$$R_{th} = \frac{T_{W,\max} - T_{in}}{Q} \tag{11}$$

where $T_{W,max}$ indicates the highest temperature of the minichannel wall.

The local wall temperature of the minichannels at the location coordinate along the helix minichannel is defined as

$$T_W(\zeta) = \frac{\int_{A_S} \rho v C_p T \, dA}{\int_{A_S} \rho v C_p \, dA} \quad (12)$$

The thermal and hydrodynamic boundary conditions assigned to all cases are shown in Table 2.

The thermal performance factor at a fixed aspect ratio for evaluating the performance of different minichannels is defined thus [33]:

$$\varepsilon = \frac{(Nu / Nu_0)}{(f / f_0)^{1/3}} \quad (13)$$

where Nu_0 and f_0 denote the Nusselt number and friction factor at a helix angle of 90° (straight minichannel), respectively. When the thermal performance factor is greater than unity, heat transfer enhancement dominates over pressure drop.

Several researchers, such as Yue et al. [34], Chai et al. [35], and Ebrahimi et al. [36], evaluated the performance of microchannels by minimizing entropy generation. The rate of entropy generation is defined as [37].

$$S_{gen} = S_{gen,T} + S_{gen,P} \quad (14)$$

$$S_{gen,T} = \frac{Q(T_{W,av} - T_f)}{T_{W,av} T_f} \quad (15)$$

$$S_{gen,P} = \frac{\dot{m}}{\rho T_f} \Delta P \quad (16)$$

where $S_{gen,T}$ and $S_{gen,P}$ are the entropy generation rates due to heat transfer and fluid friction, respectively. The definitions of the Bejan number and the augmentation entropy generation number are provided below:

$$Be = \frac{S_{gen,T}}{S_{gen,T} + S_{gen,P}} \quad (17)$$

$$\Psi = \frac{S_{gen}}{S_{gen,0}} \quad (18)$$

where $S_{gen,0}$ is the entropy generation rate at a helix angle of 90°.

2.3 Solution method and grid independence

A finite volume method was implemented to discretize the governing equations (Eqs. (1)–(4)), and the commercial software Fluent 15 was used to perform simulations. The semi-implicit method for pressure linked equations algorithm and a standard scheme were applied for pressure and velocity coupling and pressure discretization, respectively. The convective term in the momentum and energy equations were discretized via the second-order upwind method. The solution was converged at the point where the residuals of the continuity, momentum, and energy equations are smaller than 1×10^{-6}, 1×10^{-6}, and 1×10^{-9}, respectively.

To ensure the accuracy of the results and reduce simulation time, the grid independence test was performed for all models. Four sets of uniform grids with hexahedral elements were generated in the entire computational domain for all the models. For the heat sink with a helix angle = 45°, *AR* = 1.2, and *Re* = 400, for instance, the relative errors in the maximum wall temperature and pressure drop were evaluated (Table 3). Relative error is computed using the following equation [38]:

$$E_\varphi\% = \left| \frac{\varphi_{base} - \varphi}{\varphi_{base}} \right| \times 100 \quad (18)$$

where φ represents the maximum wall temperature and pressure drop. On the basis of the percentage of relative errors in Table 3, 1.890 million grids were chosen for the computations.

Table 3. Grid independence results

Number of grid × 10^{-6}	$T_{W,max}$(K)	$E_{T_{W,max}}$%	ΔP(Pa)	$E_{\Delta P}$%
0.602	310.2170	0.0822	639.0078	6.898
1.188	310.3735	0.0318	680.8090	0.808
1.890	310.4351	0.0119	681.1921	0.752
2.520	310.4721	baseline	686.3353	baseline

(a)

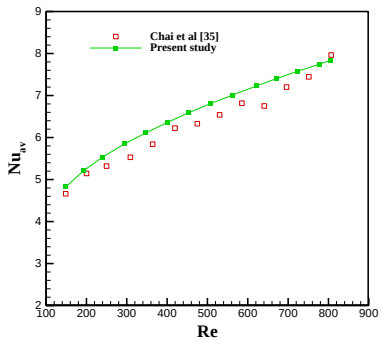

(b)

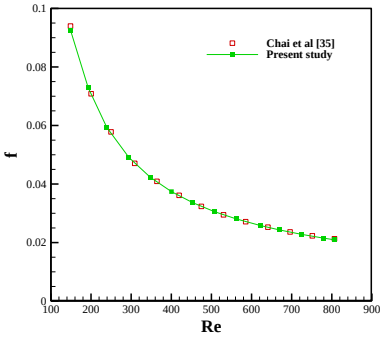

(c)

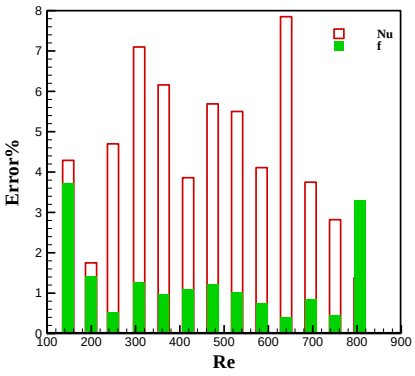

Fig. 2. Comparison of numerical solution with the experimental data of Chai et al. [35]; (a) Nu_{av}, (b) f, and (c) percentage of error.

2.4 Validation of the numerical model

For validation, the average Nusselt number and fanning friction factor were compared with the experimental data of Chai et al. [39] on straight channels with the same boundary conditions and dimensions. Fig. 2a indicates good agreement between the results in terms of the Nusselt number. The maximum deviation of the average Nusselt number is below 8%. Fig. 2b also shows strong agreement between the findings with respect to the fanning friction factor. The maximum deviation of the fanning friction factor is below 4%. The percentages of errors in the average Nusselt number and fanning friction factor are presented in Fig. 2c.

3. Results and discussion

Numerical simulations were performed to evaluate the effects of helix angle and aspect ratio on heat transfer and pressure drop in the cylindrical heat sink with helical minichannels at a Reynolds number of 100 to 900.

3.1 Effects of helix angle on heat transfer and pressure drop

Fig. 3 shows variations in the local wall temperature along the flow direction at different helix angles, $Re = 500$, and $AR = 1.2$. The local wall temperature increases along the flow direction and exhibits a similar trend at all helix angles. Such temperature decreases with decreasing helix angle in all locations. The local wall temperature of the helical minichannels is lower than that of the straight minichannel (helix angle = 90°). Additionally, the difference between the maximum and minimum temperatures of the helical minichannels is lower than that between the maximum and minimum temperatures of the straight minichannel. A helix angle of 45° enables the most uniform temperature distribution. To illustrate, the maximum wall temperature of the straight minichannel is 47.1°C, whereas the maximum wall temperature at a helix angle of 45° is 35.4°C. As a result, the local wall temperature decreases by 11.7°C—a value that is equivalent to 24.8%.

Fig. 4 presents variations in the average heat transfer coefficient with Reynolds number at different helix angles and AR = 1.2. The average heat transfer coefficient increases with Reynolds number at all helix angles, especially at high Reynolds numbers. This finding is attributed to the fact that the thickness of the thermal boundary layer decreases with increasing Reynolds number. High flow velocity improves flow mixing. Moreover, the average heat transfer coefficient at 45°, 60°, and 75° is higher than that observed at the straight minichannel. The enhancement in heat transfer coefficient is due to the generation of secondary flow by the curvature of the minichannels and the increase in heat transfer area through the enlargement in minichannel length. These results confirm that helical minichannels are the best configurations for heat dissipation in cylindrical heat sinks. As a case in point, at Re = 500, the average heat transfer coefficients at 45°, 60°, and 75° are 80.4%, 56.9% and 16.1% higher than that at the straight minichannel, respectively.

Fig. 5 displays the axial velocity contours at the middle position of the minichannels (ξ/L = 0.5) at different helix angles and Re = 500. Secondary flow

occurs at 45°, 60°, and 75°. With decreasing helix angle, centrifugal force increases, and the maximum velocity approaches the outer wall (right side) and moves outward at the middle of the minichannels' cross-sections. This phenomenon stems from the enhancement in heat transfer and flow mixing caused by the increase in secondary flow. The figure also shows that secondary flow is eliminated in the straight minichannel.

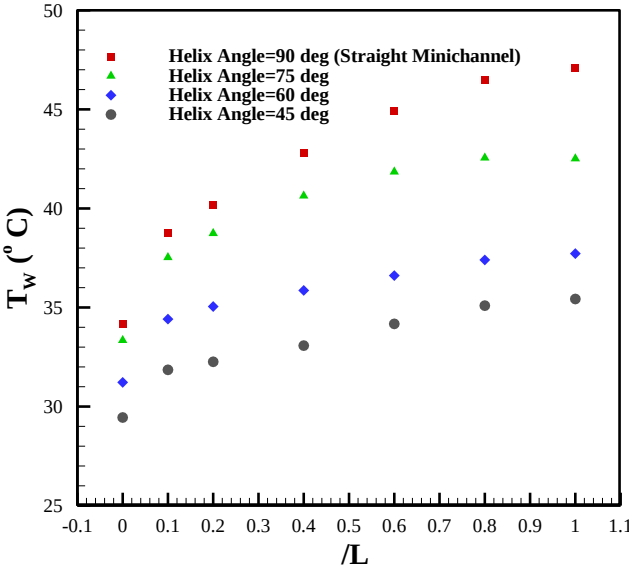

Fig. 3. Effects of axial distance on local wall temperature at different helix angles, *Re* = 500, and *AR* = 1.2.

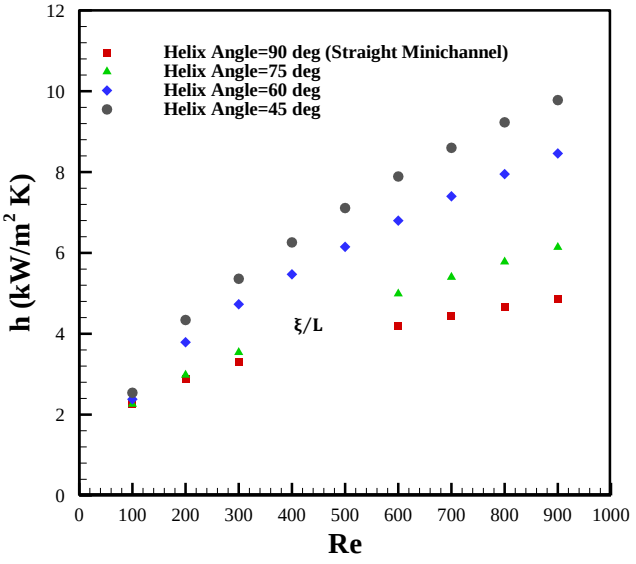

Fig. 4. Effects of Reynolds number on average heat transfer coefficient at different helix angles and *AR* = 1.2.

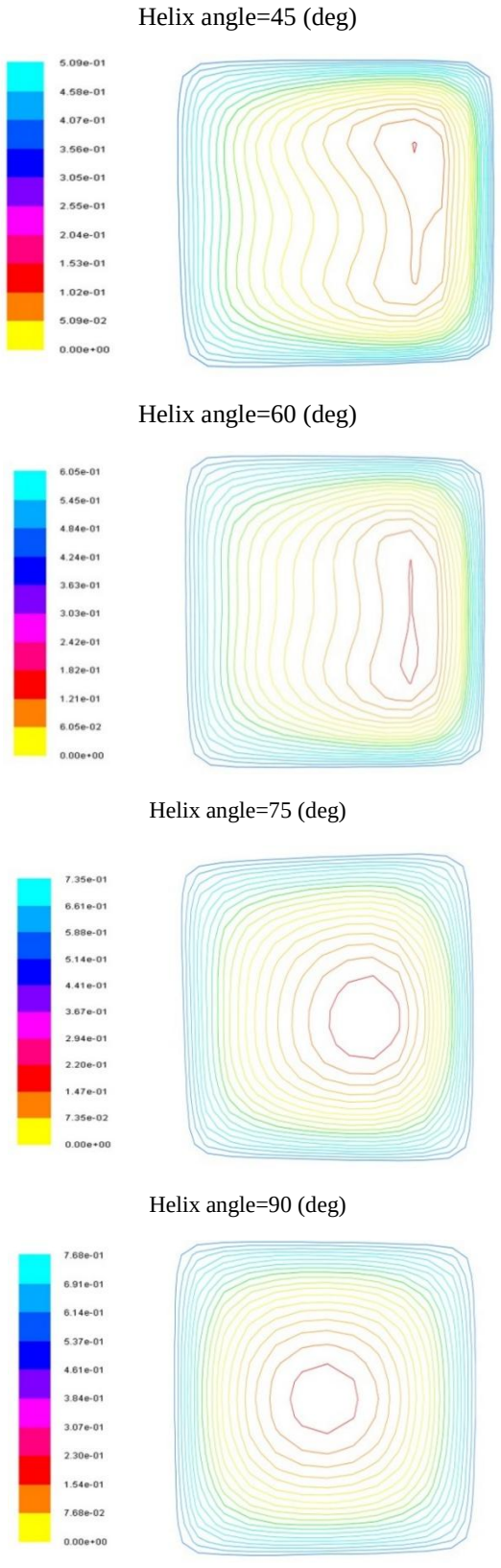

Fig. 5. Axial velocity contours at different helix angles, *Re* = 500, *AR* = 1.2, and $\frac{\xi}{L} = 0.5$.

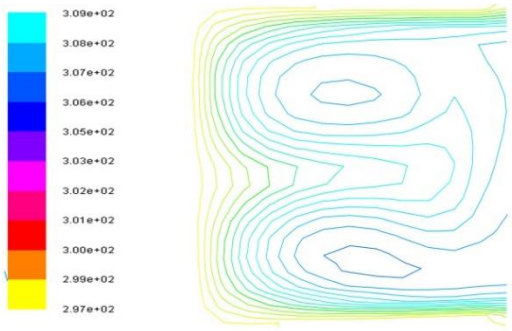

Helix angle=60 (deg)

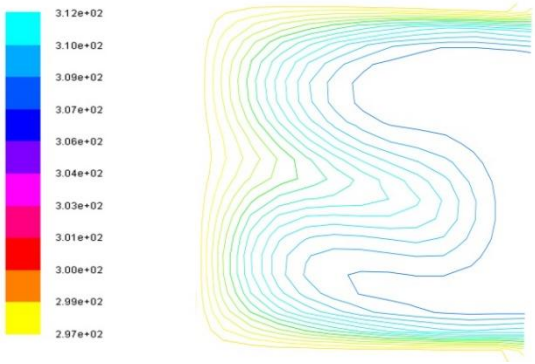

Helix angle=75 (deg)

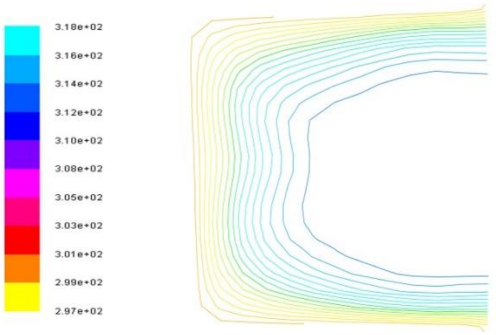

Helix angle=90 (deg)

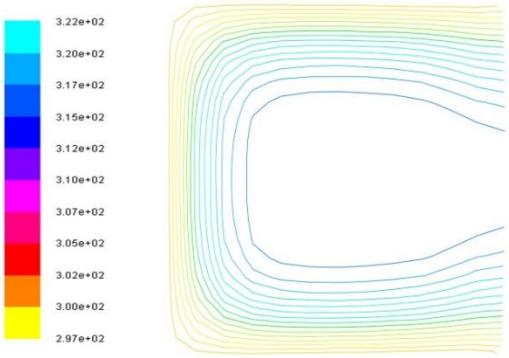

Helix angle=45 (deg)

Fig. 6. Temperature contours at different helix angles, Re = 500, AR = 1.2, and $\frac{\xi}{L} = 0.5$.

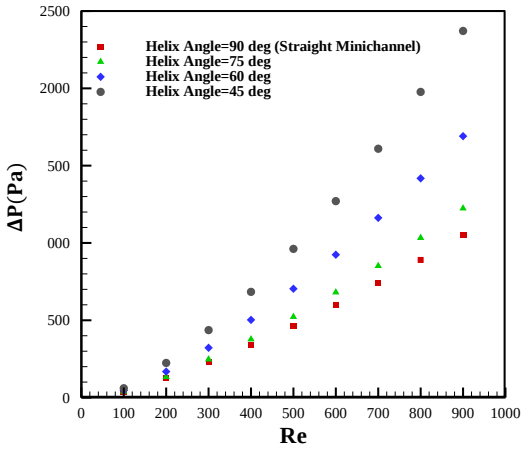

Fig. 7. Effects of Reynolds number on pressure drop at different helix angles and AR = 1.2.

The effects of helix angle on the temperature field at the middle position of the minichannels (ξ/L = 0.5) are depicted in Fig. 6. The fluid temperature near the minichannel walls is at its maximum at all helix angles. At 45°, 60°, and 75°, the maximum fluid temperature decreases relative to that in the straight minichannel. At a helix angle of 45°, for example, the maximum fluid temperature is 11 K lower than that in the straight minichannel. The temperature field is non-uniform because of the formation of vortexes at 45°, 60°, and 75° and thereby improves convective heat transfer.

Fig. 7 illustrates variations in pressure drop versus Reynolds number at different helix angles and AR = 1.2. With increasing Reynolds number, pressure drop rises at 45°, 60°, and 75° compared with the level observed in the straight minichannel. With decreasing helix angle, pressure drop rises. Pressure drop increases primarily because the helix angles reduce secondary flow and increase channel length. Reaching a high Reynolds number therefore necessitates more energy.

Fig. 8 shows variations in overall thermal resistance versus Reynolds number at different helix angles and AR = 1.2. Overall thermal resistance decreases with increasing Reynolds number and decreasing helix angle. The maximum wall temperature decreases with increasing Reynolds number at each helix angle. As an illustration, at Re = 500, the overall thermal resistance levels at 45°, 60°, and 75° are 50.1%, 39.9%, and 18.5% lower than that in the straight minichannel, respectively.

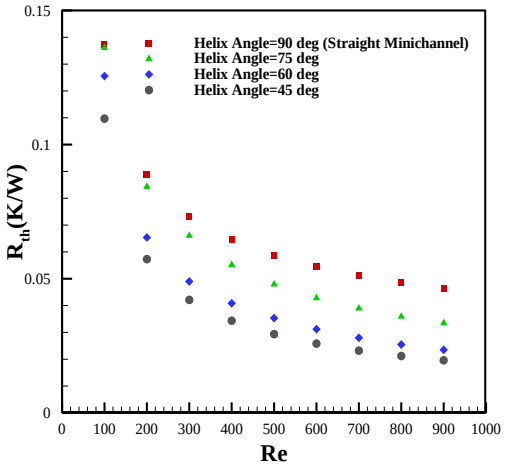

Fig. 8. Effects of Reynolds number on overall thermal resistance at different helix angles and *AR* = 1.2.

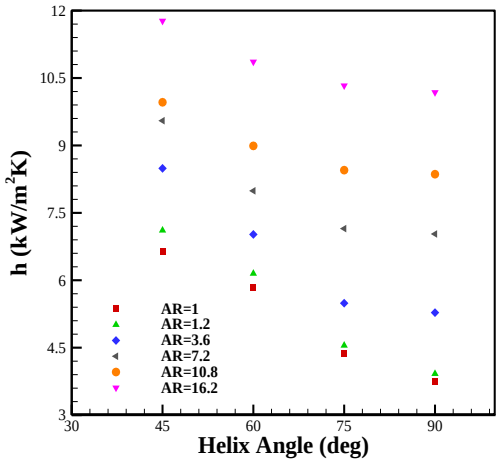

Fig. 9. Effects of helix angle on average heat transfer coefficient at different channel aspect ratios and *Re* = 500.

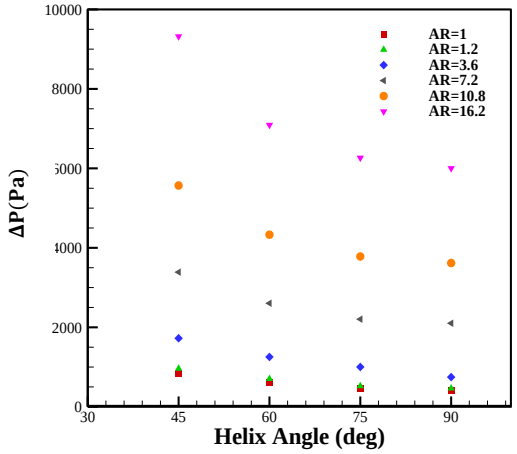

Fig. 10. Effects of helix angle on pressure drop at different channel aspect ratios and *Re* = 500.

3.2 Effects of channel aspect ratio on heat transfer and pressure drop

Fig. 9 illustrates variations in the average heat transfer coefficient versus helix angle at different aspect ratios and Re = 500 in equal cross-sectional areas. The average heat transfer coefficient increases with rising aspect ratio at all helix angles—a phenomenon related to the increase in the wetted perimeter. As mentioned previously, the average heat transfer coefficient decreases with rising helix angle because of the reduction in secondary flow and minichannel length. At aspect ratios below 7.2, the average heat transfer coefficient exhibits a sharp decrement with increasing helix angle. This behavior is especially pronounced at low aspect ratios. At high aspect ratios, however, the reduction in the average heat transfer coefficient with decreasing helix angle smoothens, indicating that the effects of helix angle on the average heat transfer coefficient decrease at high aspect ratios.

Fig. 10 shows variations in pressure drop versus helix angle at different aspect ratios and fixed cross-sectional areas. Pressure drop increases with rising aspect ratio at all helix angles, similar to the trend reported by Wang et al. [32]. The increase in aspect ratio in unchanged cross-sectional areas reduces the hydraulic diameter (Table. 1). Consequently, the water flow rate in the minichannels with small hydraulic diameters creates a high pressure drop.

Fig. 11 exhibits variations in overall thermal resistance versus helix angle at different aspect ratios and equal cross-sectional areas. Given that the maximum wall temperature increases with increasing helix angle, overall thermal resistance grows with rising helix angle. At a fixed helix angle, overall thermal resistance decreases with increasing aspect ratio. On this basis, the effects of helix angle on overall thermal resistance lessen at high aspect ratios. For instance, the overall thermal resistance at a helix angle of 45° to 90° decreases by 50.1% and 17.7% at aspect ratios of 1.2 and 16.2, respectively.

3.3 Performance evaluation criteria

On the basis of the results, heat transfer enhancement is associated with pressure drop increment in helical minichannels. We therefore evaluated the overall performance of each helical minichannel heat sink. To this end, we used the thermal performance factor and the minimization of entropy generation.

Fig. 12 (a and b) illustrates variations in the Nusselt number ratio (Nu/Nu_0) and friction

coefficient ratio (f/f_0) with Reynolds number at different helix angles. Here, Nu_0 and f_0 are the Nusselt number and friction factor of the straight minichannel, respectively. The helical minichannels improve heat transfer to levels higher than that observed in the straight minichannel (Fig. 12a). With an increment in Reynolds number, the Nusselt number ratio increases, especially at high Reynolds numbers. At a fixed Reynolds number (Re = 500), for example, the Nusselt number improves by 1.81, 1.57, and 1.16 times higher than that in the straight minichannel at 45°, 60°, and 75°, respectively. With decreasing helix angle, heat transfer enhancement is more prominent because the decrement in helix angle increases secondary flow, improves flow mixing, and enhances heat transfer. As indicated in Fig. 9b, an increasing Reynolds number elevates the friction coefficient ratio, and the rate of increase in this ratio at helix angles of 45° and 60° is higher than that at 75°. Because of the decrement in helix angle, the value of f/f_0 increases given the corresponding increase in secondary flow. The increase in f/f_0 at 45° and 60° is higher than that at 75°. The variations in the f/f_0 range at helix angles of 45°, 60°, and 75° are 1.11 to 1.6, 1.04 to 1.4 and 1 to 1.1, respectively.

Fig. 13 indicates variations in the thermal performance factor versus Reynolds number at different helix angles and AR = 1.2. The thermal performance factor is higher than unity at all helix angles. The thermal performance factor grows with increasing Reynolds number. At each Reynolds number, the thermal performance factor increases with decreasing helix angle. At a fixed Reynolds number (Re = 500), for instance, the thermal performance factors are 1.6, 1.4, and 1.3 at helix angles of 45°, 60°, and 75°, respectively. Additionally, an increase in Reynolds number from 100 to 900 enhances the thermal performance factor of the minichannels with helix angles of 45°, 60°, and 75° by 59.3%, 51.4%, and 21%, respectively.

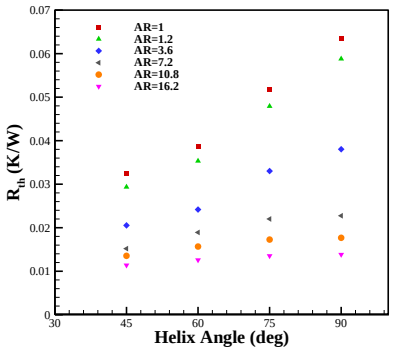

Fig. 11. Effects of helix angle on overall thermal resistance at different channel aspect ratios and *Re* = 500.

(a)

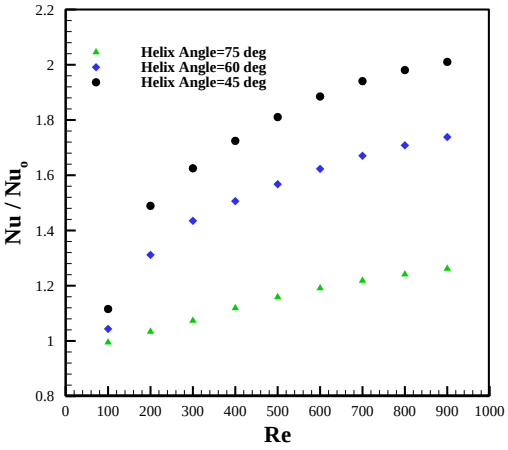

(b)

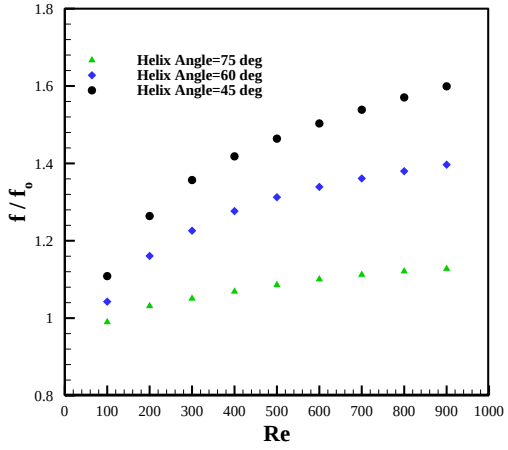

Fig. 12. Effects of Reynolds number on (a) Nusselt number ratio and (b) friction coefficient ratio at different helix angles and *AR* = 1.2.

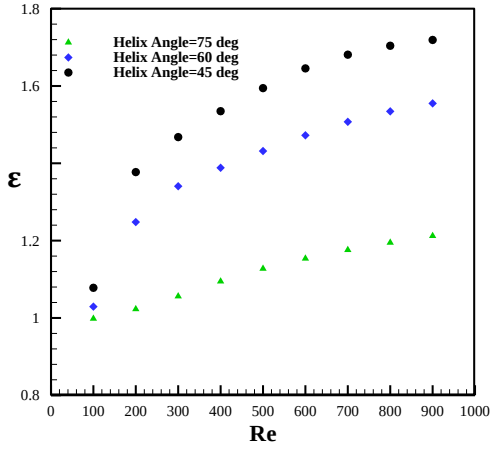

Fig. 13. Effects of Reynolds number on thermal performance factor at different helix angles and *AR* = 1.2.

Fig. 14 (a and b) shows variations in the entropy generation rate at different helix angles and AR = 1.2. With increasing Reynolds number, the thermal entropy generation rate decreases (Fig. 14a). With decreasing helix angle, such rate decreases at all Reynolds numbers, and the thermal entropy generation rate at all helix angles is lower than that observed in the straight minichannel. This finding is attributed to the increased heat transfer caused by the increment in Reynolds number and the decrement in helix angle (see Fig. 4). With increasing Reynolds number, the frictional entropy generation rate increases at all helix angles (Fig. 14b). A decrease in helix angle augments the frictional entropy generation rate; an increase in Reynolds number and a decrease in helix angle increases pressure drop. The frictional entropy generation rate is lower than the thermal entropy generation rate, with the latter dominating over the former at all helix angles and Reynolds numbers.

Fig. 14c shows the Bejan numbers at different Reynolds numbers, different helix angles, and an aspect ratio of 1.2, as a reflection of the investigation into the contribution of thermal entropy and frictional entropy generation to total entropy generation. The results showed that increasing Reynolds number and decreasing helix angle reduce the Bejan number. This finding implies that an increase in Reynolds number and a decrease in helix angle elevates the contribution of fluid friction to total entropy generation. The Bejan numbers at all helix angles are very close to unity, indicating that entropy generation is dominated by thermal entropy generation in the adopted range of Reynolds numbers and helix angles.

Fig. 15 presents variations in the augmentation entropy generation number at different helix angles and an aspect ratio of 1.2. The best performance is gained at low augmentation entropy generation numbers. Such number decreases with an increment in Reynolds number and a decrement in helix angle. The augmentation entropy generation number is also lower than unity, indicating that the heat sink with helical minichannels exhibits less irreversibility than does the heat sink with the straight minichannel.

(a)

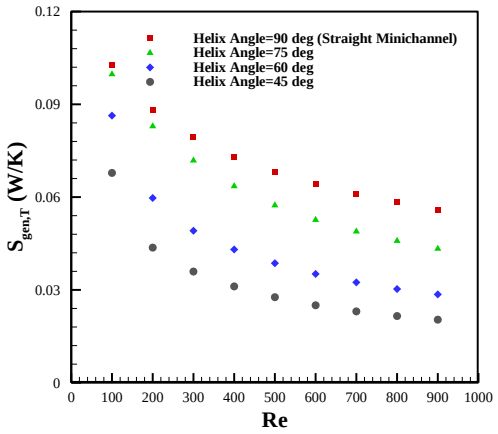

(b)

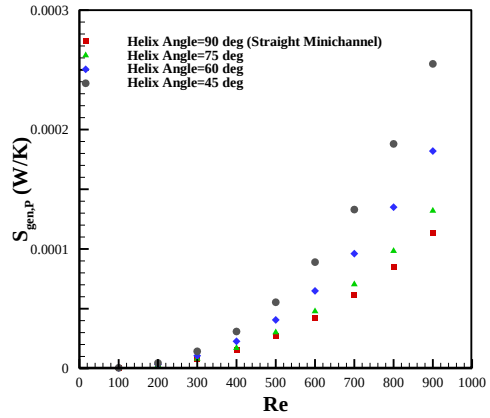

(c)

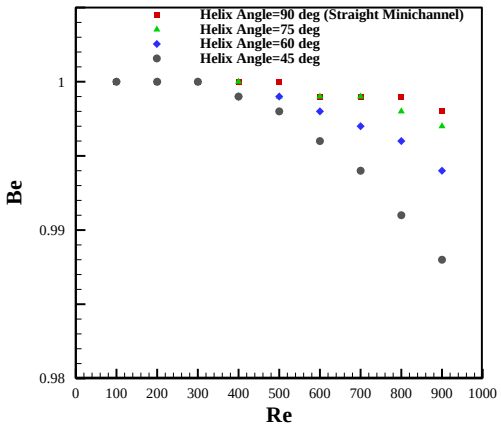

Fig. 14. Effects of the Reynolds number entropy generation rate and Bejan number at different helix angles and *AR* = 1.2; (a) thermal entropy generation, (b) frictional entropy generation, and (c) Bejan number.

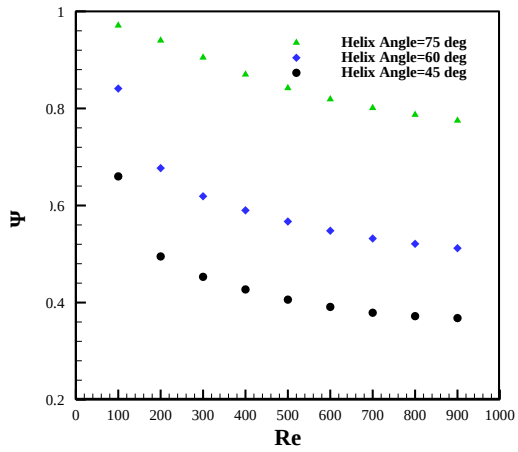

Fig. 15. Effects of helix angle on augmentation entropy generation at different helix angles and *AR* = 1.2.

(a)

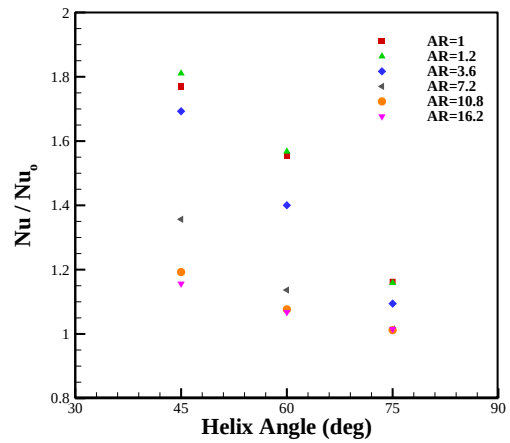

(b)

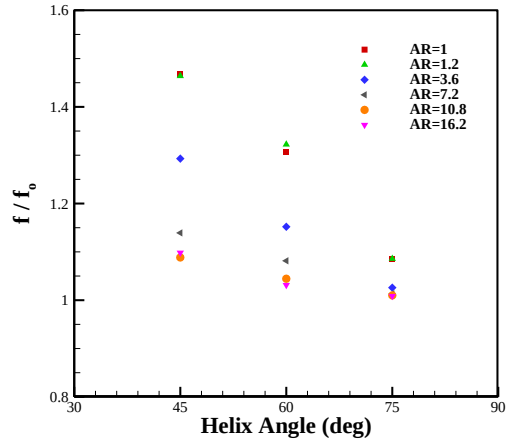

Fig. 16. Effects of helix angle on (a) Nusselt number ratio and (b) friction coefficient ratio at different aspect ratios and *Re* = 500.

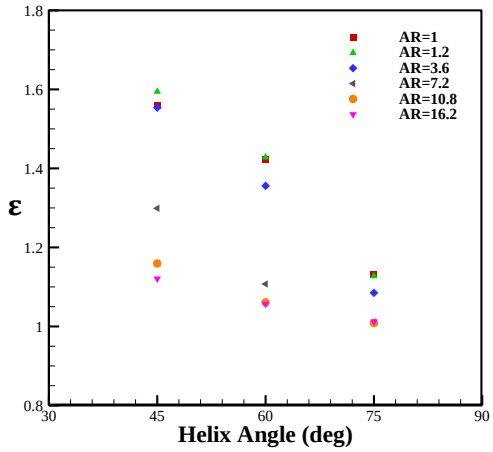

Fig. 17. Effects of helix angle on thermal performance factor at different aspect ratios and *Re* = 500.

Fig. 16 (a and b) illustrates variations in the Nusselt number ratio (Nu/Nu_0) and the friction coefficient ratio (f/f_0) with helix angle at different aspect ratios and Re = 500. As can be seen in Fig. 16a, an increase in helix angle decreases the Nusselt number ratio in the entire range of aspect ratios; however, the rate of reduction at an aspect ratio below 7.2 is higher than that at high aspect ratios. This finding means that the decrement in Nusselt number ratio at an aspect ratio of 1.2 is higher than that at other aspect ratios in all helix angles. As presented in Fig. 16b, increasing helix angle elevates the friction coefficient ratio. With an increment in aspect ratio, the friction coefficient ratio decreases.

Fig. 17 depicts variations in the thermal performance factor versus helix angle at different aspect ratios and equal cross-sectional areas. The thermal performance factor declines as helix angle increases. At aspect ratios below 7.2, the thermal performance factor sharply decreases with increasing helix angle, particularly at low aspect ratios. At high aspect ratios, however, the rate of reduction in the thermal performance factor with decreasing helix angle smoothens. For example, the thermal performance factors at helix angles of 45° to 75° decrease by 28.9% and 9.8% at aspect ratios of 1.2 and 16.2, respectively.

Fig. 18 (a and b) depicts variations in the entropy generation rate versus helix angle at different aspect ratios, equal cross-sectional areas, and Re = 500. With increasing helix angle, the thermal entropy generation rate increases because when helix angle increases, heat transfer decreases (Fig. 18a). With a decrement in aspect ratio, the thermal entropy generation increases because when aspect ratio decreases, heat transfer decreases (Fig. 9).

(a)

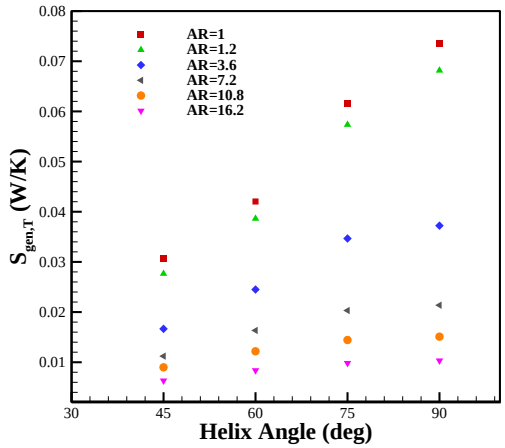

(b)

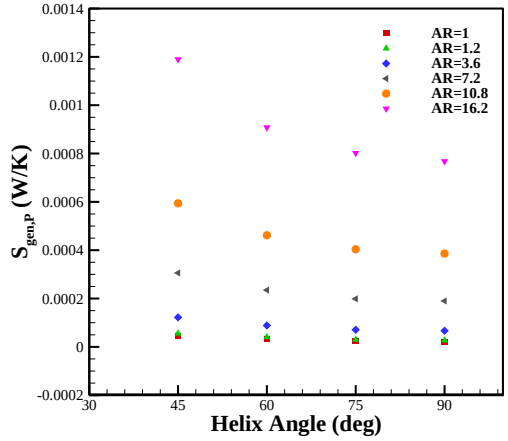

(c)

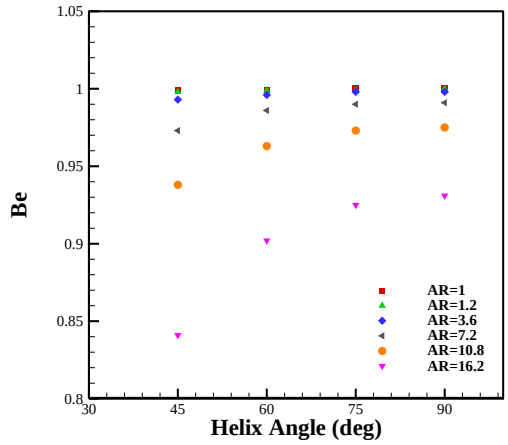

Fig. 18. Effects of the helix angle on entropy generation rate and Bejan number at different aspect ratios and Re = 500; (a) thermal entropy generation, (b) frictional entropy generation, and (c) Bejan number.

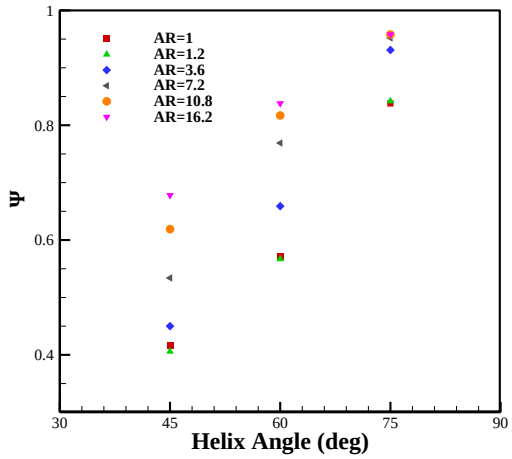

Fig. 19. Effects of helix angle on augmentation entropy generation number at different aspect ratios and Re = 500.

The thermal entropy generation rate sharply increases at low aspect ratios ($AR < 7.2$). With an increment in helix angle, the frictional entropy generation rate decreases, and with increasing aspect ratio, the frictional entropy generation rate increases (Fig. 18b). Fig. 18c shows variations in the Bejan number versus helix angle at different aspect ratios, equal cross-sectional areas, and Re = 500. The results showed that with increasing helix angle and decreasing aspect ratio, the Bejan number increases. At a fixed helix angle and decreasing aspect ratio, the contribution of frictional entropy generation to total entropy generation decreases. Such contribution is very close to unity at low aspect ratios ($AR < 7.2$).

Fig. 19 graphically represents variations in the augmentation entropy generation number versus helix angle at different aspect ratios, equal cross-sectional areas, and Re = 500. The augmentation entropy generation number increases with an increment in helix angle. With increasing aspect ratio, the augmentation entropy generation number increases at all helix angles. The heat sink with an aspect ratio of 1.2 exhibits a low augmentation entropy generation number and the best thermodynamic performance.

4. Conclusions

Heat transfer and laminar fluid flow in a novel cylindrical heat sink with helical minichannels were investigated numerically by a finite volume method. The effects of helix angle, aspect ratio, and Reynolds number were also examined. On the basis of the

numerical results, the following conclusions were derived:

- The heat sink with helical minichannels has a lower local wall temperature and overall thermal resistance than does the heat sink with a straight minichannel.
- When helix angle decreases, the length of minichannels and secondary flow increase, thereby enhancing heat transfer and reducing pressure drop.
- With decreasing helix angle, the average heat transfer coefficient increases relative to that observed in the straight minichannel. At Re = 500 and AR = 1.2, for instances, heat transfer improves by 80.4%, 56.9%, and 16.1% at helix angles of 45°, 60°, and 75°, respectively.
- An increasing aspect ratio at equal cross-section areas of the minichannels increases the average heat transfer coefficient and pressure drop at all helix angles.
- At low aspect ratios ($AR < 7.2$), a reduction in helix angles considerably affects the average heat transfer coefficient and overall thermal resistance.
- The thermal performance factor is higher than unity at all helix angles. It increases with rising Reynolds number and declining helix angle.
- At high aspect ratios, the effects of helix angle on the thermal performance factor decrease. For example, the thermal performance factor at a helix angle of 45° to 75° decreases by 28.9% and 9.8% at aspect ratios of 1.2 and 16.2, respectively.
- The entropy generation minimization method revealed that an aspect ratio of 1.2 enables the best performance, which is also achieved with decreasing helix angle.

Nomenclature

A_C	Cross-sectional area of minichannel, m^2
A_S	Convection heat transfer area, m^2
AR	Minichannel aspect ratio
Be	Bejan number
C_P	Specific heat transfer, J/kg K
D	Heat sink diameter, m
D_h	Hydraulic diameter, m
d	Heat source diameter, m
f	Friction factor
H	Minichannel height, m
h	Heat transfer coefficient, W/m^2 K
k	Thermal conductivity, W/m K
L	Minichannel length, m
$\dot{m}$	Mass flow rate, kg/s
Nu	Nusselt number
P	Pressure, Pa
PP	Pumping power, W
Q	Heat gain by water, W
R_{th}	Total thermal resistance, K/W
Re	Reynolds number
S_{gen}	Total entropy generation rate, W/K
$S_{gen,P}$	Frictional entropy generation rate, W/K
$S_{gen,T}$	Heat transfer entropy generation rate, W/K
Re	Reynolds number
S	Heat sink length, m
T	Temperature, K
V	Velocity, m/s
W	Minichannel width, m
Greek symbols	
μ	Dynamic viscosity, Pa.s
ρ	Density, kg/m^3
ε	Thermal performance factor
ζ	Location coordinate along a helix minichannel , m
Ψ	Augmentation entropy generation number
Subscripts	
av	Average
f	Fluid
in	Inlet
max	Maximum
w	Wall

References

[1]. Y. Fan, P. Seng Lee, B. Wah Chua, Investigation on the influence of edge effect on flow and temperature uniformities in cylindrical oblique-finned minichannel array, International Journal of Heat and Mass Transfer, 70, 651–663, (2014).

[2]. D.B. Tuckerman, R.F.W. Pease, High-performance heat sinking for VLSI, IEEE Electron Device Letters, 2 (5), 126-129, (1981).

[3]. W. Qu, I. Mudawar, Experimental and Numerical Study of Pressure Drop and Heat Transfer in a Single-Phase Microchannel Heat Sink, International Journal of Heat and Mass Transfer, 45(12) 2549–2565, (2002).

[4]. X.L. Xie, Z.J. Liu, Y.L. He, W.Q. Tao, Numerical study of laminar heat transfer and pressure drop characteristics in a water-cooled minichannel heat sink, Applied Thermal Engineering, 29 (1), 64–74, (2009).

[5]. Y. Sui, C.J. Teo, P.S. Lee, Y.T. Chew, C. Shu, Fluid flow and heat transfer in wavy microchannels, International Journal of Heat and Mass Transfer, 53 (13-14), 2760–2772, (2010).

[6]. H.A. Mohammed, P. Gunnasegaran, N.H. Shuaib, Influence of channel shape on the thermal and hydraulic performance of microchannel heat sink, International Communications in Heat and Mass Transfer, 38 (4), 474–480, (2011).

[7]. H.A. Mohammed, P. Gunnasegaran, N.H. Shuaib, Numerical simulation of heat transfer enhancement in wavy microchannel heat sink, International Communications in Heat and Mass Transfer, 38 (1) 63–68, (2011).

[8]. Y. J. Lee, P. S. Lee, S. K. Chou, Numerical Study of Fluid Flow and Heat Transfer in the Enhanced Microchannel With Oblique Fins, Journal of Heat Transfer, 135 (4), 041901-0419010, (2013).

[9]. L. Chai, G.D. Xia, H. S. Wang, Parametric study on thermal and hydraulic characteristics of laminar flow in microchannel heat sink with fan-shaped ribs on sidewalls– Part 1: Heat transfer, International Journal of Heat and Mass Transfer, 97, 1069–1080, (2016).

[10]. G. Xie, Y. Li, F. Zhang, B. Sunden, Analysis of micro-channel heat sinks with rectangular-shaped flow obstructions, NUMERICAL HEAT TRANSFER, 69 (4), 1–17, (2016).

[11]. X. W. Zhu, Y. H. Fu, J. Q. Zhao, L. Zhu, Three-dimensional numerical study of the laminar flow and heat transfer in a wavy-finned heat sink filled with AL2O3/ethylene glycol-water nanofluid, NUMERICAL HEAT TRANSFER, 69 (2), 1–14, (2015).

[12]. M. Bovand, S. Rashidi, J.A. Esfahani, Heat transfer enhancement and pressure drop penalty in porous solar heaters: Numerical simulations, Solar Energy, 123, 145–159, (2016).

[13]. M. Bashi, S. Rashidi, J.A. Esfahani, Exergy analysis for a plate-fin triangular duct enhanced by a porous material, Applied Thermal Engineering, 110, 1448-1461, (2017).

[14]. S. Rashidi, N. Moghadas Zade, J. Abolfazli Esfahani, Thermo-fluid performance and entropy generation analysis for a new eccentric helical screw tape insert in a 3D tube, Chemical Engineering and Processing: Process Intensification, 117, 27-37, (2017).

[15]. S. Rashidi, M. Akbarzadeh, R. Masoodi, E.M. Languri, Thermal-hydraulic and entropy generation analysis for turbulent flow inside a corrugated channel, International Journal of Heat and Mass Transfer, 109, 812-823, (2017).

[16]. C.J. Ho, L.C. Wei, Z.W. Li, An experimental investigation of forced convective cooling performance of a microchannel heat sink with Al2O3/water nanofluid, Applied Thermal Engineering, 30 (2-3), 96–103, (2010).

[17]. Y. J. Lee, P. K. Singh, P. S. Lee, Fluid flow and heat transfer investigations on enhanced microchannel heat sink using oblique fins with parametric study, International Journal of Heat and Mass Transfer, 81, 325–336, (2015).

[18]. B. Rimbault , C. T. Nguyen , N. Galanis, Experimental investigation of CuO-water nanofluid flow and heat transfer inside a microchannel heat sink, International Journal of Thermal Sciences, 84, 275-292, (2014).

[19]. H. Zirakzadeh, A.R. Mashayekh,H. Noori Bidgoli, M. Ashjaee, Exprimental investigation of heat transfer in a novel heat sink by means of alumina nanofluids, Heat Transfer Research, 43(8), 709–720, (2012).

[20]. Y.J. Lee, P.S. Lee, S.K. Chou, Enhanced Thermal Transport in Microchannel Using Oblique Fins, Journal of Heat Transfer, 134 (10), 101901, (2012).

[21]. S.M. Peyghambarzadeh, S.H. Hashemabadi, A.R. Chabi, M. Salimi, Performance of water based CuO and Al2O3 nanofluids in a Cu–Be alloy heat sink with rectangular microchannels, Energy Conversion and Management, 86, 28–38, (2014).

[22]. M. Khoshvaght-Aliabadi, F. Nozan, Water cooled corrugated minichannel heat sink for electronic devices: Effect of corrugation shape,

International Communications in Heat and Mass Transfer, 76, 188–196, (2016).

[23]. Y. Fan, P. S. Lee, L.W. Jin, B. W. Chua, A simulation and experimental study of fluid flow and heat transfer on cylindrical oblique-finned heat sink, International Journal of Heat and Mass Transfer, 61 (1), 62–72, (2013).

[24]. Y. Fan, P. S. Lee, L.W. Jin, B. W. Chua, Experimental investigation on heat transfer and pressure drop of a novel cylindrical oblique fin heat sink, International Journal of Thermal Sciences, 76, 1-10, (2014).

[25]. Z. Azizi, A. Alamdari, M.R. Malayeri, Convective heat transfer of Cu–water nanofluid in a cylindrical microchannel heat sink, Energy Conversion and Management, 101, 515–524, (2015).

[26]. Z. Azizi, A. Alamdari, M.R. Malayeri, Thermal performance and friction factor of a cylindrical microchannel heat sink cooled by Cu-water nanofluid, Applied Thermal Engineering 99, 970–978, (2016).

[27]. B. Xu., K. T, Ooi., C. Mavriplis., M. E. Zaghloul, Evaluation of viscous dissipation in liquid flow in microchannels, Journal of Micromechanics and Microengineering, 13(1), 53-57,(2002).

[28]. L. Chai, G. Xia, M. Zhou, J. Li, J. Qi, Optimum thermal design of interrupted microchannel heat sink with rectangular ribs in the transverse microchambers, Applied Thermal Engineering, 51, 880–889, (2013).

A. M. Adham, N. Mohd-Ghazali, R. Ahmad, Performance Optimization of a Microchannel Heat Sink Using the Improved Strength Pareto Evolutionary Algorithm (SPEA2), Journal of Engineering Thermophysics, 24 (1), 86–100, (2015).

[29]. Y.T. Yang, H.Sen Peng, Numerical Study of Thermal and Hydraulic Performance of Compound Heat Sink, Numerical Heat Transfer, 55 (5), 432–447, (2009).

[30]. G. Xie, Zh. Chen, B. Sunden,W. Zhang, Numerical Predictions of the Flow and Thermal Performance of Water-Cooled Single-Layer and Double-Layer Wavy Microchannel Heat Sinks, Numerical Heat Transfer, 63 (3), 201–225, (2013).

[31]. H. Wang, Zh. Chen, J. Gao, Influence of geometric parameters on flow and heat transfer performance of micro-channel heat sinks, Applied Thermal Engineering, 107, 870–879, (2016).

[32]. M. Khoshvaght-Aliabadi, A. Alizadeh, An experimental study of Cu–water nanofluid flow inside serpentine tubes with variable straight-section lengths, Experimental Thermal Fluid Science, 61, 1–11, (2015).

[33]. Y. Yue, Sh. K. Mohammadian, Y. Zhang, Analysis of performances of a manifold microchannel heat sink with nanofluids, International Journal of Thermal Sciences, 89, 305-313, (2015).

[34]. L. Chai, G.D. Xia, H.S. Wang, Parametric study on thermal and hydraulic characteristics of laminar flow in microchannel heat sink with fan-shaped ribs on sidewalls – Part 3: performance evaluation, International Journal of Heat and Mass Transfer, 97, 1091–1101, (2016).

A. Ebrahimi, F. Rikhtegar, A. Sabaghan, E. Roohi, Heat transfer and entropy generation in a microchannel with longitudinal vortex generators using nanofluids, Energy, 101, 190-201, (2016).

[35]. G. D. Xai, Y.L. Zhia, Z.Z. Cui, Characteristics of entropy generation and heat transfer in a microchannel with fan-shaped reentrant cavities and internal ribs, Science China Technological Sciences, 56 (7), 1629–1635, (2013).

[36]. D.D. Ma, G.D. Xia, Y.F. Li, Y.T. Jia, J. Wang, Effects of structural parameters on fluid flow and heat transfer characteristics in microchannel with offset zigzag grooves in sidewall, International Journal of Heat and Mass Transfer, 101, 427–435, (2016).

[37]. L. Chai, G. Xia, L. Wang, M. Zhou, Z. Cui, Heat transfer enhancement in microchannel heat sinks with periodic expansion–constriction cross-sections, International Journal of Heat and Mass Transfer, 62 (1), 741-751, (2013).